

Protomagnetar and black hole formation in high-mass stars

M. Obergaulinger¹, M.Á. Aloy¹

¹ *Departament d'Astronomia i Astrofísica, Universitat de València,*

Edifici d'Investigació Jeroni Munyoz, C/Dr. Moliner, 50, E-46100 Burjassot (València), Spain

26 September 2018

ABSTRACT

Using axisymmetric simulations coupling special relativistic MHD, an approximate post-Newtonian gravitational potential and two-moment neutrino transport, we show different paths for the formation of either protomagnetars or stellar mass black holes. The fraction of prototypical stellar cores which should result in collapsars depends on a combination of several factors, among which the structure of the progenitor star and the profile of specific angular momentum are probably the foremost. Along with the implosion of the stellar core, we also obtain supernova-like explosions driven by neutrino heating and hydrodynamic instabilities or by magneto-rotational effects in cores of high-mass stars. In the latter case, highly collimated, mildly relativistic outflows are generated. We find that after a rather long post-collapse phase (lasting $\gtrsim 1$ sec) black holes may form in cases both of successful and failed supernova-like explosions. A basic trend is that cores with a specific angular momentum smaller than that obtained by standard, one-dimensional stellar evolution calculations form black holes (and eventually collapsars). Complementary, protomagnetars result from stellar cores with the standard distribution of specific angular momentum obtained from prototypical stellar evolution calculations including magnetic torques and moderate to large mass loss rates.

Key words: Supernovae: general - gamma-ray bursts: general

1 INTRODUCTION

Supported by a host of observations of supernova (SN) explosions, gamma-ray bursts (GRBs), their remnants, and the compact objects they leave behind, current theory of stellar core collapse considers a variety of outcomes for the post-collapse evolution of the burnt-out cores of massive stars ($M_{\text{ZAMS}} \gtrsim 8 M_{\odot}$). Plausible scenarios involve the formation of a proto-neutron star (PNS), from whose inner core a shock wave is launched and fails to reach the outer layers of the star but stalls inside the core. Neutrino heating, hydrodynamic instabilities, and, possibly, other mechanisms such as rotation and magnetic fields act against the accretion of the surrounding shells increasing the mass of the PNS. The balance between these effects may lead to a SN explosion in which the accretion flows are shut down and the PNS at the centre gradually transforms into a neutron star. It is also conceivable that the asymmetric geometry of the explosion runs parallel to continuing accretion and, hence, the PNS grows beyond the maximum mass supported against self-gravity and, finally, collapses to a black hole (BH). The latter outcome is probably inevitable if no SN occurs at all. Irrespective of the failure or success of a previous SN explosion, high-energy transients are possible even after BH formation, in particular if rapid rotation allows for a long GRB in the collapsar model.

The first scenario (SN explosion and NS formation) seems likely particularly for stars in the lower range of masses (for recent studies, see, e.g., O'Connor & Ott 2011; Janka 2012; Ugliano et al. 2012; Sukhbold et al. 2016; Nakamura et al. 2015; Bruenn

et al. 2016), while we might encounter conditions favouring BH formation with or without SN explosion among stars with higher masses. The former studies suggest a fairly complex dependence of the final outcome on the progenitor conditions rather than, say, a clear threshold at a certain mass. We explore this complex landscape focusing on low metallicity models, some of which have been traditionally considered as precursors of collapsars (Woosley & Heger 2006). We examine in detail the post-collapse evolution of five models of core collapse based on two $35 M_{\odot}$ progenitors taken from stellar evolution calculations (see Sect. 2, Sect. 3, and Sect. 4 for our models, results, and conclusions, respectively). We vary the angular momentum profile and the magnetic field strength in the progenitor star and perform axisymmetric simulations including special-relativistic MHD and two-moment neutrino transport. A similar study has been performed by Burrows et al. (2007) and Dessart et al. (2008). However, we improve on that paper in several aspects (neutrino transport, inclusion of special relativistic MHD and the treatment of gravity).

2 MODELS

We performed axisymmetric simulations of the coupled evolution of the stellar gas, its magnetic fields, and the neutrinos emitted by the core solving the equations of special-relativistic magnetohydrodynamics and neutrino transport. To this end, we use the Eulerian finite-volume code described in Just et al. (2015), which we

previously had applied in core-collapse modelling (Obergaulinger et al. 2014). The most important extension w.r.t. the latter study is the inclusion of heavy-lepton neutrinos and the pair processes (electron-positron annihilation and nucleonic bremsstrahlung) producing them. We included the effects of gravity in the neutrino transport in the $O(v)$ -plus formulation of Endeve et al. (2012).

We use the equation of state (EoS) of Lattimer & Swesty (1991) with an incompressibility of $K_3 = 220$ MeV for densities above $\rho = 6 \times 10^7$ g cm $^{-3}$, which allows for a maximum baryonic neutron-star mass of $M_{\text{m;bry}} \approx 2.45 M_\odot$ (we note that all masses quoted in this article will be baryonic masses.) At lower densities, the EoS contains electrons and positrons, photons, and baryons.

We simulate two stars with zero-age main-sequence masses of $M_{\text{ZAMS}} = 35 M_\odot$, one of which is considered as a prototype progenitor of a collapsar. The pre-collapse states of stellar models 350C and 350B are the results of spherical stellar-evolution computations of Woosley & Heger (2006) that include rotation and an approximation to a dynamo driven by rotation and the associated magnetic transport of angular momentum (Spruit 2002). The models differ only in their mass-loss rate, whose values translate to total stellar masses of $M_{350C} = 28.1 M_\odot$ and $M_{350B} = 21.2 M_\odot$ at collapse. The structure of the two cores differs considerably, particularly at mass coordinates outside $2 M_\odot$ (Fig. 1), i.e., in the regions whose accretion will determine the final fate of the SN shock wave and the compact remnant. The progenitor star 350C possesses a non-convective iron core in (quasi-)nuclear statistical equilibrium (NSE) of $M_{\text{Fe};350C} \approx 2.1 M_\odot$ surrounded by a region of about $4 M_\odot$ in which convection maintains a flat entropy profile (see Fig. 1). In model 350B, the transition from the iron core to the convective layers is made up of two distinct shells, and the jumps of entropy and density at the first interface (at $m \approx 2.3 M_\odot$) are less than at the corresponding interface in model 350C, and the next, more gradual, transition is at a rather large mass coordinate of $m \approx 3.2 M_\odot$. Further differences can be found in the rotational profile: model 350B possesses a smooth, monotonically increasing profile of specific angular momentum, j . On the other hand, model 350C displays a drop of j by a factor of 5 at a mass coordinate of $2.1 M_\odot$, such that the inner and outer regions of the core have a larger and smaller j than model 350B at the same mass coordinates, respectively.

We simulated versions of the former model with its original rotational profile and either weak or very strong magnetic fields (models 350C-R0, 350C-Rw, and 350C-Rs, respectively) as well as a version of the model in which we reduced the rotational rate by a factor 4 and included a weak magnetic field (model 350C-Sw). To this set, we added model 350B-R0, a simulation of core 350B with the original rotational profile and magnetic field. We initialized models 350C-R0 and 350B-R0 using the profiles of the radial and toroidal components of the stellar-evolution model. These fields are fairly strong with maximum strengths $b_{\text{max}}^r \approx 5 \times 10^{10}$ G and $b_{\text{max}}^\phi \approx 10^{12}$ G (model 350C) and $b_{\text{max}}^r \approx 2 \times 10^{10}$ G and $b_{\text{max}}^\phi \approx 9 \times 10^{11}$ G (model 350B). The artificial magnetic fields included in models 350C-Rw, 350C-Rs, and 350C-Sw are defined in terms of the vector potential, \tilde{A} , of Suwa et al. (2007)

$$(A^r, A^\theta, A^\phi) = [2(r^3 + r_0^3)]^{-1} (b_0 r_0^3 r \sin \theta, 0, b_0 r_0^3 r^2 \cos \theta). \quad (1)$$

We set the radius parameter $r_0 = 10^8$ cm and the normalizations such that the poloidal and toroidal components of the magnetic field at the origin are $b^{\text{pol,tor}} = 10^8$ G or 10^{10} G for all models except for 350C-Rs, for which $b^{\text{pol,tor}} = 10^{12}$ G. The exact value of the field strength in the former class of models is not important because the field remains dynamically insignificant in our simulations. However,

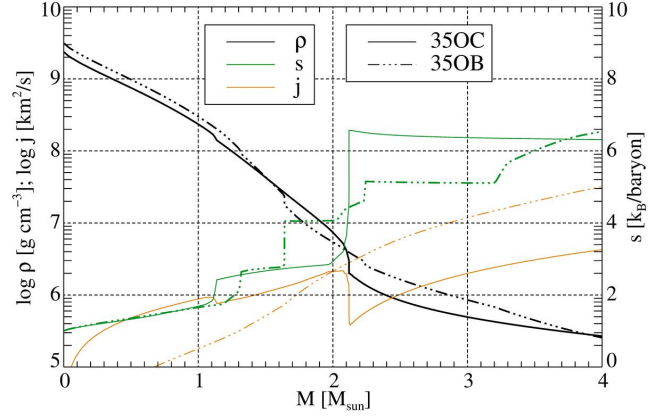


Figure 1. Pre-collapse profiles of mass density (black), specific entropy (green), and specific angular momentum (orange) of models 350C (solid lines) and 350B (dashed-triple-dotted lines) as functions of enclosed mass.

we cannot exclude that such weak fields grow to relevant strengths by processes (magnetorotational instability, turbulent dynamos, see Mösta et al. 2015) acting at small scales below our grid resolution. The computational domain extends up to $R_{\text{out}} = 1.4 \times 10^{10}$ cm, spans latitudes in the range $[0^\circ, 180^\circ]$ and it is covered with $n_r \times n_\theta = 400 \times 128$ zones in spherical coordinates (logarithmically spaced in the radial direction and uniform in the angular direction). The neutrino spectrum is discretized in 10 log-spaced bins.

3 RESULTS

O’Connor & Ott (2011) demonstrated that very compact cores, characterized by a high value of the compactness, $\xi_m = \frac{m/M_\odot}{R_m/1000 \text{ km}}$, where R_m is the radius enclosing a total mass m (usually taken to be $2.5 M_\odot$), tend to resist shock revival and yield failed SN explosions that lead to BH formation by accretion onto the PNS. The values of $\xi_{2.5;350C} = 0.49$ and $\xi_{2.5;350B} = 0.56$ place our cores in a marginal regime where explosions can be expected to be quite difficult to achieve. Nevertheless, as the time evolution of the shock radii (Panel (a) of Fig. 2) demonstrates, all models eventually achieve shock revival, albeit driven by distinct mechanisms. The explosions are very asymmetric, thus allowing for ongoing equatorial accretion onto the PNS, which, therefore, might reach the maximum mass that can be supported against gravity and then collapse to a BH. Panels (b) and (c) present the time evolution of the total (internal, kinetic, magnetic and gravitational) energy and the mass for all the matter that is unbound, i.e., has a positive total energy. The former quantity is a proxy of the explosion energy. We find a broad range of energies and masses. We note particularly energies in excess of 10^{51} erg and still growing when the simulations are ended. Only model 350B-R0 shows a lower explosion energy, but we expect it to exceed 10^{50} erg if the model were run for a longer time. In all cases, we find ejecta masses $\gtrsim 0.2 M_\odot$, which may grow further on longer time scales.

The high compactness of the cores 350C and 350B translates into PNSs that are quite massive already at their formation and grow strongly afterwards (Panel (d) of Fig. 2), exceeding $2 M_\odot$ after only 200 ms except for model 350C-Rs, for which the PNS mass reaches a maximum of $M_{\text{PNS}} \approx 1.95 M_\odot$ at $t \approx 450$ ms and then decreases again. For models of core 350C, the increase slows down once the interface of the iron core has been accreted, which happens

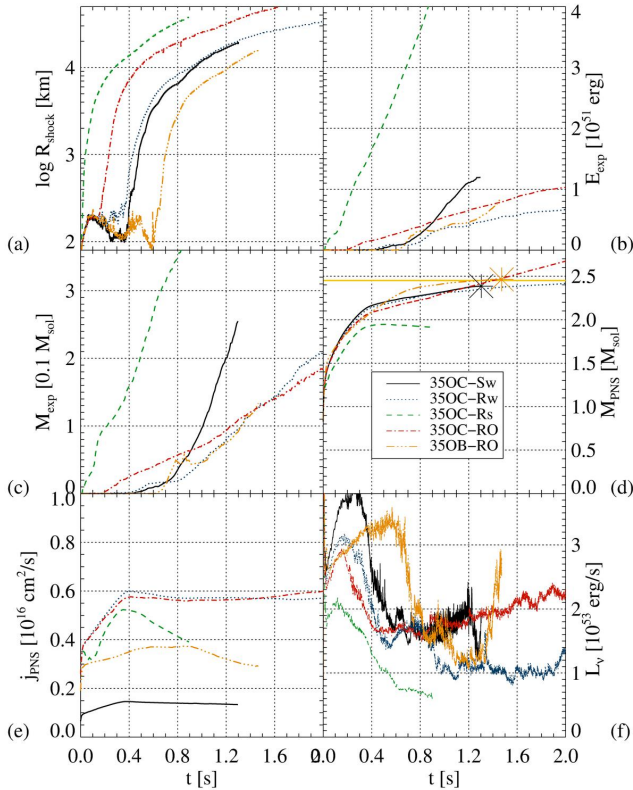


Figure 2. Panel (a): maximum shock radii of our models as a function of post-bounce time. Panels (b,c): total energy and mass of all unbound material. Panels (d,e): masses and specific angular momentum of the PNS, defined as all mass exceeding a density threshold of $\rho_{\text{PNS}} = 10^{12} \text{ g cm}^{-3}$. The horizontal line shows the maximum mass of a cold-non-rotating neutron star supported by our EoS, and asterisks mark the instants of collapse to a BH. Panel (f): total (all flavours) neutrino luminosities.

at $t \sim 300 \text{ ms}$. A similar behaviour was found in 2D; e.g., Cerdá-Durán et al. (2013) and in 3D models; e.g., Hanke et al. (2013). Model 350C-Sw undergoes BH collapse after $\sim 1.2 \text{ sec}$ with a PNS mass slightly below the EoS limit (the difference can be attributed to our approximate GR potential). We note that the decrease of the mass accretion rate (the derivative of the curves in the figure) is less pronounced for model 350B-R0 than for models 350C as the former model starts at this point to accrete the still fairly dense intermediate layer outside of the comparably weak density jump at $m \approx 2.3 M_{\odot}$. Hence, the PNS of model 350B-R0 exceeds the maximum mass of a cold, non-rotating NS rather quickly. Even though the PNS mass grows to $M_{\text{PNS}} \approx 2.6 M_{\odot}$, it is temporarily stabilized by thermal and rotational support, until it collapses to a BH too. In addition, all of the PNSs possess fairly high rotational energy and specific angular momentum (Panel (e)) of the order of several $10^{15} \text{ cm}^2 \text{ sec}^{-1}$. The highest values are found in the rapidly rotating versions of model 350C. Models 350C-Rw and 350C-R0 maintain a roughly constant level of $j \approx 5.7 \times 10^{15} \text{ cm}^2 \text{ sec}^{-1}$ after $t \approx 0.4 \text{ sec}$, whereas the decrease of the PNS mass of model 350C-Rs, setting in around that time, is accompanied by a drop of its specific angular momentum. Model 350C-Sw behaves similarly to the former two models and shows a flat specific angular momentum, though at a much lower level. Finally, the comparably high specific angular momentum that model 350B-R0 possesses outside a mass coordinate of $m = 2.3 M_{\odot}$ (see Fig. 1) yields a moderate rise of j , which, does not exceed that of models 350C-Rw and 350C-R0, though.

The neutrino luminosities (Panel (f) of Fig. 2) reflect the mass accretion history with a drop corresponding to the accretion of the interface of the iron core. Rapidly rotating models consistently emit less energy in neutrinos than their slowly rotating counterparts. Many studies of the explosion mechanism of CCSNe (e.g. Murphy & Burrows 2008; Nordhaus et al. 2010; Hanke et al. 2012; Janka 2012; Suwa et al. 2016) found a positive correlation between the neutrino luminosity of a core and its tendency towards explosion with shock revival setting in if a critical luminosity that depends on, among other factors, the mass accretion rate of the core, is exceeded. The similar times of explosion found in model 350C-Rw and model 350C-Sw seem to contradict this connection. An even lower luminosity can be found in models 350C-Rs and 350C-R0, which are also the first to explode, whereas model 350B-R0 with the second lowest luminosity of all models explodes last. To resolve these apparent disagreements with theoretical expectations, we have to turn to the two-dimensional structure of the models as we shall see below in the discussion of the individual models.

The explosion of model 350C-Sw is closest to the standard paradigm of neutrino-driven shock revival aided by hydrodynamic instabilities. After stagnating and receding, the shock starts to expand once the surface of the iron core has been accreted. The process is dominated by the highly stochastic dynamics of convection and the standing accretion shock instability (SASI) creating large-scale bubbles of high entropy which evolve into outflows of a degree of collimation that varies with time, but is on average less pronounced than in other models. We also note that the ejecta show, due to their origin in highly stochastic processes a strong north-south asymmetry (see Panel (a) of Fig. 3). Downflows remain active between these bubbles, feeding the growth of the PNS. Consequently, the PNS collapses to a BH after $t \sim 1.2 \text{ sec}$. We point out that the neutrino emission is highly aspherical and the amount of energy deposition varies strongly with time and latitude, leading to a highly variable rate of injection of mass and energy into the northern and southern outflows. By the time of BH formation, the core shows a roughly spherical shape with a radius $R_{\text{PNS}} \approx 17 \text{ km}$ (Panel (a) of Fig. 4) and a small spin parameter $a \approx 0.17$. The high compactness of the core translates the moderate rotational and magnetic energies into a high surface-averaged angular velocity in excess of $\Omega_{\text{PNS}} \gtrsim 1000 \text{ s}^{-1}$ and surface fields of several 10^{14} G .

Prior to the onset of explosion, the shock surface and the neutrino-spheres are oblate due to the strong centrifugal support in model 350C-Rw. Consequently, the gain layer at the pole is exposed to an enhanced neutrino flux. This effect locally compensates for the reduction of the total neutrino luminosity mentioned above (cf. Panel (f) of Fig. 2). Along the poles where rotational support is weakest, L_{ν} is even stronger than in model 350C-Sw. Thus, though residing quite deep in the gravitational well, the polar regions of the gain layer satisfy the conditions for an explosion as soon as the iron core interface is accreted and the mass accretion rate and ram pressure at the shock decrease. We note that the latter variables are already before that point smaller than in model 350C-Sw. For this reason, the shock does not retreat as much as in that model. An explosion develops whose geometry is similar to that of model 350C-Sw (Panel (b) of Fig. 3). The explosion occurs while matter is still falling onto the PNS at low latitudes, allowing the PNS to grow. Compared to model 350C-Sw, the time of shock revival and the evolution of the maximum shock radius are almost unchanged, but both their mass and energy grow slower (Panels (b,c) of Fig. 2). The degree of collimation of the outflow, while varying with time, is higher than that of model 350C-Sw, in particular towards the end of the simulation. A rotationally stabilized quasi-toroidal structure

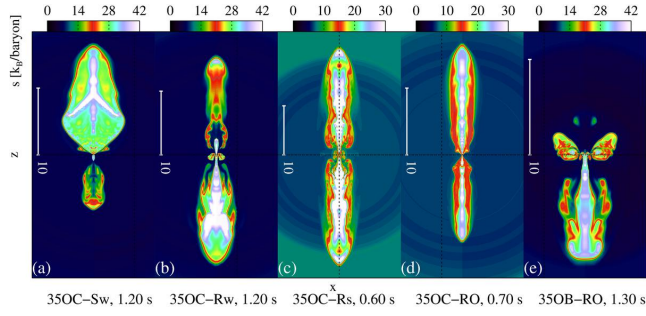


Figure 3. Maps of the specific entropy of the cores of all models at different times after core bounce as listed in the panels. The length scale of the panels is represented by a ruler of length 10^4 km.

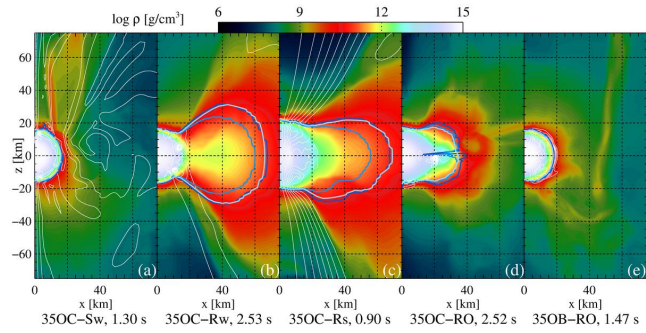


Figure 4. Mass density of the cores of all models prior to the end of the simulations (names and times listed in the panels). The magnetic field is represented by field lines (white) and blue lines show the three neutrinospheres.

extending at the equator to ≈ 60 km (compared to a polar radius of ≈ 16 km) surrounds the inner core (see Panel (b) of Fig. 4). This equatorial torus contains a fairly large fraction of the total angular momentum, its surface rotates rapidly ($\Omega_{\text{PNS}} > 2000 \text{ s}^{-1}$) and is strongly magnetized ($b_{\text{PNS}} > 10^{14.5} \text{ G}$).

If rapid rotation is combined with a strong magnetic field (model 350C-Rs), a bipolar explosion develops almost immediately after bounce (Fig. 3, Panel (c)). Along the poles, the shock wave never even stalls. The explosion does not result from the reduction of the mass accretion rate because shock expansion starts long before the surface of the iron core has fallen onto the PNS, i.e., in the phase when \dot{M} is greater than at the time of shock expansion of models 350C-Sw and 350C-Rw. Later on, mass accretion, occurring mainly via equatorial downflows is weaker and is after $t \approx 400$ ms even entirely quenched by the expanding ejecta. Consequently, the PNS mass is by the end of the simulation $\approx 0.2 M_{\odot}$ smaller than in the other two models, and we do not expect the PNS to collapse to a BH for many dynamical time scales. The explosion is not caused mainly by neutrinos, whose luminosity is weaker than in any other model. Instead, the ejecta are generated magneto-rotationally. By the end of the simulation, the outflows have reached velocities of $v_r \sim c/3$, and the speed of the jet head is close to $c/5$. The oblate geometry of the PNS is even more pronounced than in the models discussed so far (Panel (c) of Fig. 4). The surface is at $\Omega_{\text{PNS}} \approx 1000 \text{ s}^{-1}$ and $b_{\text{PNS}} \lesssim 10^{15} \text{ G}$, i.e., model 350C-Rs rotates slower and is more magnetized than model 350C-Rw. The axisymmetry of our models restricts them compared to three-dimensional models (Mösta et al. 2014) since first, they do not observe the quenching of the accretion flow by the ejecta and, second, their jets exhibit 3d instabilities absent in our models.

The behaviour of model 350C-RO (panel (d) of Fig. 3) lies in between those of models 350C-Rw and model 350C-Rs. Shock revival occurs at $t \approx 200$ ms due to neutrino heating concentrated at the poles. Strong magnetic fields partially suppress lateral motions in the gain layer. Consequently, fluid elements are not as likely to leave the region of maximum heating rate sideways towards the equator as in model 350C-Rw. The explosion caused by neutrino energy deposition aided by magnetic fields shares many characteristics with standard neutrino-driven explosions such as a certain degree of stochasticity that manifests itself in north-south asymmetry of the ejecta. The strong magnetic field transports angular momentum from the interior of the PNS to its outer layers, which as a consequence possess an excess of rotational support and assume an oblate form (Panel (d) of Fig. 4). At the termination of the simulation, the PNS is very massive ($M_{\text{PNS}} \gtrsim 2.6 M_{\odot}$), but not very compact (the polar and equatorial radii are between 16 and 40 km) due to its fast rotation (the effective spin parameter is $a \approx 0.6$), and it does not seem to be at the verge of forming a BH. Its surface rotation and magnetic field are characterized by high values of $\Omega_{\text{PNS}} \lesssim 2000 \text{ s}^{-1}$ and $b_{\text{PNS}} \gtrsim 5 \times 10^{14} \text{ G}$.

With a magnetic field too weak for a magneto-centrifugal explosion, model 350B-RO explodes similarly to model 350C-Rw, albeit much later ($t \sim 600$ s). We refer to Panel (e) of Fig. 3 showing the morphology of the ejecta at late times. The delay is caused by the high mass accretion rates and ram pressures at the shock persisting until the accretion of the interface at $m = 2.3 M_{\odot}$ (cf. Fig. 1). Because at most locations in the core the initial density is higher than in model 350C, the PNS mass grows rapidly and reaches $M_{\text{PNS}} = 2.45 M_{\odot}$ already at $t \approx 1.2$ s. At that point, the PNS (at a spin parameter $a \approx 0.45$) is rather compact and moderately oblate with radii between 16 (poles) and 22 km (Panel (e) of Fig. 4). It rotates at $\Omega_{\text{PNS}} > 3000 \text{ s}^{-1}$ and possesses a field strength of $b_{\text{PNS}} \sim 6 \times 10^{14} \text{ G}$. The model forms a moderately rotating BH after about 1.4 s.

4 DISCUSSION AND CONCLUSIONS

To assess their viability as candidates for supernova explosions and as progenitors of long GRBs, we studied the collapse and the post-bounce evolution of the cores of stars of initial masses of $M_{\text{ZAMS}} = 35 M_{\odot}$ with different degrees of rotation and magnetic fields in neutrino-MHD simulations. Our five simulations show very distinct dynamics: (1) explosions within the standard neutrino-driven paradigm of supernova theory, but followed by collapse to a BH; (2) rapid rotation concentrating neutrino emission along the rotational axis and generating bipolar explosion; (3) early magneto-rotational explosions launching moderately relativistic outflows.

All explosions have a very prolate morphology. The energies and masses of the ejecta differ strongly among models, with the most violent explosion, viz. one launched by the magneto-rotational mechanism, exceeding an energy of $E_{\text{exp}} = 4 \times 10^{51} \text{ erg}$ and a mass of $M_{\text{exp}} = 0.38 M_{\odot}$ at the end of the simulation, while the others achieve energies of the order of $E_{\text{exp}} = 10^{51} \text{ erg}$ that are still growing when we had to terminate the computation.

In most cores, accretion onto the PNS goes on after the onset of explosion, thus making a later collapse to a BH quite likely, and in two models BH collapse was actually found. In such a case, we expect that the models with the most rapid rotation might produce a second energy release in which hyperaccretion onto the newly formed BH drives another generation of outflows along the rotational axis into the low-density funnel left behind by the ini-

tial outflows. Dessart et al. (2008) found that model 350C is very susceptible to early magneto-rotational explosions that inhibit the growth of the PNS mass and make a later collapse to a BH unlikely, thus diminishing the prospects of a collapsar-type progenitor. Indeed, the reduction of the rotation rate (model 350C-Sw) as well as a different profile of the core (model 350B-R0) allow for BH formation and, thus, an evolution within the collapsar scenario. Our strongly magnetized models suggest similar conclusions, but indicate a greater possibility for GRBs powered by a PM central engine (Metzger et al. 2011; M11 hereafter). Even though simulations on longer times are required to settle this issue, we already observe that the way towards the fiducial conditions assumed in M11 is more complex than sketched by the former authors. The main reasons for the discrepancy arise from two facts. First, the equatorial accretion along with bipolar mass loss, both of variable strength, are active throughout the post-bounce time here presented. Consequently, the mass of the PNS may change either increasing (350C-R0) or slightly decreasing (350C-Rs). It should be noted that without the restriction of axisymmetry, the dynamics of the accretion flows feeding the PNS might be considerably more complex and BH formation might be less likely. Second, the PNS shape of potential PMs is very oblate (i.e., not spherical). Some of the key parameters in the PM model are the period (P_0), the radius and the mass of the PNS at the moment of *birth* of the PM (which can be taken ~ 10 s post bounce when the contraction of the PNS practically ceases in the M11 model), as well as the poloidal component of the magnetic field on the surface of the PNS. The time evolution of all of them during the first 2 s post bounce does not follow the simple paths sketched in M11. We estimate for models 350C-R0 and 350C-Rs values $P_0 \simeq 0.1 - 0.25$ ms extrapolating the evolution of the PNS after 50 ms post bounce. These values are smaller than the ones computed for stable and isolated neutron stars ($P_0 \gtrsim 1$ ms) of smaller masses than the PNSs we consider here (e.g., Strobel et al. 1999 make their estimates for a mass of $1.35 M_\odot$). Likewise, M11 assume that the magnetic field energy is a fraction $\epsilon_B \sim 10^{-3}$ of the gravitational energy of the PNS. Our potential PM models show $\epsilon_B \gtrsim 10^{-2}$. However, the poloidal field at the PNS surface is smaller than assumed in M11. For model 350C-Rs, $b_{\text{PNS}}^{\text{pol}} \simeq b_{\text{PNS}}^{\text{tor}} \sim 5 \times 10^{14}$ G, while for model 350C-R0 $b_{\text{PNS}}^{\text{pol}} \simeq 0.1 b_{\text{PNS}}^{\text{tor}} \sim 5 \times 10^{13}$ G. Finally, we note that potential PM models display an early phase of magnetic field amplification where b_{PNS} quickly ($t \simeq 0.4$ sec) settles to a value $\sim 5 \times 10^{14}$ G. Models evolving into collapsars need $t \simeq 1$ sec to arrive to similar values of b_{PNS} , and once at that level, they display variations in strength by factors ~ 3 within timescales of 100 ms.

We close with a few comments on the shortcomings and uncertainties of our current study. While general-relativistic versions of our models might produce slightly different results, even shift the border between SN explosion and BH collapse somewhat, we think that the pseudo-relativistic potential we chose is a rather accurate approximation and affects only the criteria for, but not the existence of the scenarios summarized above. In this context, we mention in particular that our approach does not include energy losses due to gravitational waves. However, the rotational frequencies required for this effect to play a role exceed those of our models, and hence we deem its neglect insignificant. Our treatment of neutrino-matter interactions can be improved by using more recent opacity models, but tentatively expect that the uncertainty coming from that source is also more in the realm of minor quantitative shifts in the parameter space rather than a complete change of our conclusions. The most important limitation is axisymmetry, as three-dimensional effects

might considerably modify the topology of the flows (Winteler et al. 2012; Mösta et al. 2014). While very interesting, three-dimensional long-term simulations of several models are still very challenging computationally and, thus, a topic for future research.

5 ACKNOWLEDGEMENTS

We thank O. Just and Th. Janka for valuable help. We acknowledge the support from the European Research Council (grant CAMAP-259276), and the partial support of grants AYA2015-66899-C2-1-P, AYA2013-40979-P and PROMETEO-II-2014-069 and computational time on the clusters *Pirineus*, *Picasso*, *MareNostrum*, and *Tirant* under grants AECT-2016-1-0008, AECT-2016-2-0012, and AECT-2016-3-0005 of the Spanish Supercomputing Network.

REFERENCES

- Bruenn S. W., Lentz E. J., Hix W. R., Mezzacappa A., Harris J. A., Messer O. E. B., Endeve E., Blondin J. M., Chertkow M. A., Lingerfelt E. J., Marronetti P., Yakunin K. N., 2016, *ApJ*, 818, 123
- Burrows A., Dessart L., Livne E., Ott C. D., Murphy J., 2007, *ApJ*, 664, 416
- Cerdá-Durán P., DeBrye N., Aloy M. A., Font J. A., Obergaulinger M., 2013, *ApJ*, 779, L18
- Dessart L., Burrows A., Livne E., Ott C. D., 2008, *ApJ*, 673, L43
- Endeve E., Cardall C. Y., Mezzacappa A., 2012, *ArXiv e-prints*
- Hanke F., Marek A., Müller B., Janka H.-T., 2012, *ApJ*, 755, 138
- Hanke F., Müller B., Wongwathanarat A., Marek A., Janka H.-T., 2013, *ApJ*, 770, 66
- Janka H.-T., 2012, *Annual Review of Nuclear and Particle Science*, 62, 407
- Just O., Obergaulinger M., Janka H.-T., 2015, *MNRAS*, 453, 3386
- Lattimer J. M., Swesty F. D., 1991, *Nuclear Physics A*, 535, 331
- Metzger B. D., Giannios D., Thompson T. A., Bucciantini N., Quataert E., 2011, *MNRAS*, 413, 2031
- Mösta P., Ott C. D., Radice D., Roberts L. F., Schnetter E., Haas R., 2015, *Nature*, 528, 376
- Mösta P., Richers S., Ott C. D., Haas R., Piro A. L., Boydston K., Abdikamalov E., Reisswig C., Schnetter E., 2014, *ApJ*, 785, L29
- Murphy J. W., Burrows A., 2008, *ApJ*, 688, 1159
- Nakamura K., Takiwaki T., Kuroda T., Kotake K., 2015, *PASJ*, 67, 107
- Nordhaus J., Burrows A., Almgren A., Bell J., 2010, *ApJ*, 720, 694
- Obergaulinger M., Janka H.-T., Aloy M. A., 2014, *MNRAS*, 445, 3169
- O'Connor E., Ott C. D., 2011, *ApJ*, 730, 70
- Spruit H. C., 2002, *A&A*, 381, 923
- Strobel K., Schaab C., Weigel M. K., 1999, *A&A*, 350, 497
- Sukhbold T., Ertl T., Woosley S. E., Brown J. M., Janka H.-T., 2016, *ApJ*, 821, 38
- Suwa Y., Takiwaki T., Kotake K., Sato K., 2007, *PASJ*, 59, 771
- Suwa Y., Yamada S., Takiwaki T., Kotake K., 2016, *ApJ*, 816, 43
- Ugliano M., Janka H.-T., Marek A., Arcones A., 2012, *ApJ*, 757, 69
- Winteler C., Käppeli R., Perego A., Arcones A., Vasset N., Nishimura N., Liebendörfer M., Thielemann F.-K., 2012, *ApJ*, 750, L22
- Woosley S. E., Heger A., 2006, *ApJ*, 637, 914